RSC Applied Polymers

ROYAL SOCIETY OF CHEMISTRY

PAPER

View Article Online
View Journal | View Issue

Cite this: *RSC Appl. Polym.*, 2024, **2**, 71

Direct ink writing of polyimide aerogels for battery thermal mitigation†

Ciera E. Cipriani, [a] Donald A. Dornbusch,[b] Stephanie L. Vivod *[b] and Emily B. Pentzer *[a,c]

Aerogels, which are ultralightweight and highly porous materials, are excellent insulators with applications in thermal management, acoustic impedance, and vibration mitigation. Aerogels have huge potential in the aerospace industry as a lightweight solution for thermally insulating electronic components which are confined within a small volume. However, the application of aerogels is currently hampered by the primary processing method of molding, which is costly, time-consuming, requires tooling, and limits geometric complexity. The extrusion-based 3D printing method of direct ink writing (DIW) provides an avenue to move past these constraints. However, rheology modifying additives are commonly used to make a sol printable, which may negatively impact the performance of the product aerogel. Here, we report the DIW of pure polyimide aerogels by subjecting the sol to mild heating (60 °C for 5 min) to promote gelation and produce a printable ink. This approach yielded printed aerogels with comparable microstructural, mechanical, and thermal properties to cast aerogels. The printed aerogel is stable up to 500 °C and has potential for high temperature applications relevant to the aerospace industry. We highlight the utility of this system by printing a bespoke enclosure to insulate a heating plate as a model for batteries; even at a plate temperature of 120 °C, the surface of the 8 mm thick aerogel maintained ambient temperature, indicating excellent inhibition of heat transfer. Additionally, a printed aerogel casing for a solid-state electrolyte coin cell battery resulted in a tenfold increase in ionic conductivity sustained for 100 min. This novel, simple method for 3D printing aerogels opens exciting opportunities to move beyond the geometric limitations of molding to expand the application space of these ultralightweight materials.

Received 11th October 2023,
Accepted 7th December 2023

DOI: 10.1039/d3lp00200d

rsc.li/rscapplpolym

Introduction

Aerogels are a key material in advanced applications because of their unique combination of extremely low density (ranging from 1 to as low as 0.001 g cm^{-3}),[1] high porosity (up to and sometimes exceeding 99%),[1–3] high specific surface area (500–1000 m^2 g^{-1}),[1] and mechanical strength.[4,5] Since their introduction in 1931,[6] aerogels have found application across a variety of disciplines, including energy storage devices,[7] acoustic insulators,[8,9] thermal insulators,[10–15] vibration mitigation systems,[16] catalysts and catalyst supports,[17–19] and Cherenkov detectors.[20] The light weight of aerogels makes them appealing for space applications, where each kilogram of mass can cost tens of thousands of dollars to launch.[21] Aerogels have been critical to space missions, finding use as collectors for cosmic dust,[4,20,22–24] spacesuit insulation,[25] antenna substrates,[26] and insulation for battery packs on the Mars Sojourner rover,[25,27] to name a few examples.

Aerogels are prepared by a sol–gel process, which involves forming a colloidal suspension (sol) which reacts over time to form a network (gel). Once the network is formed, the gel is dried by removing solvent without collapsing the solid structure, resulting in highly porous solids.[2] Primary drying methods include critical point drying or freeze drying, although some studies have demonstrated ambient pressure drying by strengthening the nanostructure[28,29] or modifying the surface to enable the nanostructure to "spring back" after drying.[1,2,30–32] Aerogels have a diverse array of compositions, including silica,[1,13,20,22,30–32] titania,[33] and other metal oxides,[34–36] along with carbon,[17,37–41] chalcogenides,[42–45] polymers,[4,5,8,26,46–50] and biological materials.[10,51–54] Of these, polymer aerogels offer unique opportunities to tailor chemical composition, with polyimide aerogels being of particular interest due to their combination of good mechanical performance

[a]*Department of Materials Science and Engineering, Texas A&M University, 3003 TAMU, College Station, Texas 77843, USA. E-mail: emilypentzer@tamu.edu*
[b]*NASA Glenn Research Center, 21000 Brookpark Road, Cleveland, Ohio 44135, USA*
[c]*Department of Chemistry, Texas A&M University, 3255 TAMU, College Station, Texas 77843, USA*

† Electronic supplementary information (ESI) available. See DOI: https://doi.org/10.1039/d3lp00200d

and high thermal stability.[3] For example, polyimide aerogels can be up to 500 times stronger than silica aerogels,[55] have elastic modulus values up to 42.7 MPa,[56] and are stable to extended heating at 400 °C.[5]

Despite their increasing use, applications of aerogels are currently limited by available manufacturing techniques, primarily molding. Molding requires the separate, often costly, manufacture of the mold itself, which is not conducive to rapid customization for a desired geometry. The geometry of the molded aerogel is also limited by the ability to remove the gel from the mold. New approaches are needed to manufacture aerogels with tailored geometries and rapid prototyping, *e.g.*, for custom fit around multiple components; this is especially important given the high concentration of electronic components within a relatively small volume in aircraft and spacecraft. Conformal geometries were key to the success of using aerogels as substrates for patch antennas[26] and electronics insulation in the Mars Sojourner rover.[25,27] Looking forward, the use of custom-fit aerogels for lightweight thermal insulation of batteries can facilitate electric vehicle and electric aviation applications. Solid-state batteries are particularly promising due to their wide temperature stability resulting from the removal of volatile organic liquid electrolytes.[57] However, lower room-temperature ionic conductivity and poor interfacial contact currently limits the use of solid-state electrolytes for high performance applications. These limitations can be mitigated by increasing the operating temperature, thus increasing the ionic conductivity.[58] As such, the ability to maintain high temperature throughout operation is critical for harnessing solid-state batteries for electric aviation, and lightweight, custom-fit aerogel insulators have potential to address this concern.

Expanding access to non-moldable 3D shapes will enable aerogels to insulate more complex arrangements of electronic components. Recent efforts to move beyond molding have focused on additive manufacturing methods such as stereolithography,[59–62] inkjet printing,[62–64] and direct ink writing (DIW),[38,41,62,65–67] to name a few. Of these, DIW is particularly useful because it is inexpensive, simple to use, has minimal instrumentation requirements, and allows for high control over the feedstock composition. Although many studies have been published on the DIW of gels,[68–72] DIW of aerogels is rare. The major challenge of using DIW to print polymer aerogels is achieving the requisite rheology of the sol. Specifically, a feedstock ink should be a high-viscosity yielding fluid, meaning that it exhibits solid-like behavior at rest, but transitions to a fluid-like state upon application of shear.[73–80] The ink should also be shear-thinning so that its apparent viscosity decreases with increased shear rate.[73–79] These factors enable extrusion from a syringe for DIW printing. After extrusion, the ink should regain its high viscosity to maintain the printed shape. This increase in viscosity with decreased shear is termed thixotropy.[74,75,78,81,82] Generally, such performance is observed near the gelation point of the polyimide. Therefore, optimizing the chemistry and timing the printing process can be challenging. A sol which gels quickly is ideal for achieving printability in a short time; however, the sol should not gel so quickly that it solidifies in the syringe. On the other hand, a slow-gelling sol provides a large window for loading into a syringe for printing, but it also increases processing time and makes it difficult to print large structures (*e.g.*, this may require multiple syringes of ink). Finally, if the material chemistry is application-specific, control over the gelation time by changing the chemistry is limited.

To address these challenges of achieving the requisite rheology for DIW printing, a variety of rheology-modifying additives have been incorporated into sols, including cellulose nanocrystals,[83] graphene,[84] multi-walled carbon nanotubes,[84] bacterial cellulose,[85] fumed silica,[86] and silica aerogel particles.[87] Although additives may be useful for imparting additional functionality, they can also impact the desirable properties of the aerogel, modifying the porosity, density, and optical transparency compared to the pure aerogel. Only a handful of studies report DIW approaches for the printing of pure aerogels, *i.e.*, without particle additives. The Du group reported a resorcinol-formaldehyde sol–gel ink which could be printed by DIW, then carbonized.[38] The resulting carbon aerogel possessed nanoscale porosity and a high specific surface area of 631 $m^2 g^{-1}$. To prepare the ink, the resorcinol-formaldehyde colloidal dispersion was heated to 60 °C for 4 h, then 80 °C for 1 h. The structure was treated with hydrochloric acid during printing so that the extruded shape could be maintained. The same group later achieved the printing of resorcinol-formaldehyde inks without hydrochloric acid treatment;[41] this was made possible by modifying the gelation process to improve rheology for DIW, aging the inks for 2 to 3 h at 80 °C. In the same work, the Du group heated silica sol to 60 °C for 5.5 h to prepare an ink for printed silica aerogel, along with a polyimide-based ink which was printed without heat treatment. However, the polyimide sol did not possess the rheological behavior required for DIW on its own, so the ink was printed into a water bath to promote solidification. As a result, the printed polyimide structures were inconsistent with cast aerogels: the printed aerogel pores were on the micron scale, whereas cast aerogels had nanoscale porosity. Other approaches to DIW of pure polyimide aerogels have harnessed additional processing steps such as ball milling[88] or post-printing imidization by chemical treatment,[46] heating, or ultraviolet light exposure.[89] The process of directly printing polyimide sol using an off-the-shelf printing setup is critical to expanding the applications of these important materials.

The goal of the present work was to 3D print aerogels which are chemically and physically identical to cast aerogels, with the added benefit of 3D printing to make custom geometries which are challenging or impossible to produce using traditional molding methods. To enable stacking of many layers and realize fully 3D printed pure polyimide aerogels with high dimensional fidelity, rheological optimization is necessary. Herein, we report that a mild heat treatment can be used to promote the gelation of a polyimide sol and achieve the rheological performance necessary for DIW printing to produce

pure polyimide aerogels with similar microstructural, mechanical, and thermal properties to the cast system. An illustration of this new processing approach is provided in Fig. 1A. Through this technique, either high-resolution or high-throughput printing can be achieved using the same sol, depending on the extent of gelation and nozzle size. The printed aerogel has comparable morphology, thermal properties, and mechanical performance to its cast counterpart. Furthermore, we illustrate that the printed aerogels possess excellent thermal insulation performance for applications such as bespoke housings for electronic components. This is demonstrated by an experiment imitating the insulation of a battery during heat generation, where aerogel was printed to enclose a heating plate in an 8 mm thick layer. As the plate heated to 120 °C, the aerogel maintained ambient temperature on its surface. A printed aerogel casing for a solid-state electrolyte coin cell battery elucidated the usefulness of these structures for improving ionic conductivity *via* thermal insulation. Polyimide aerogels can thus be printed in complex, conformal geometries to make custom-fit insulators with potential for improving electronics performance in demanding environments.

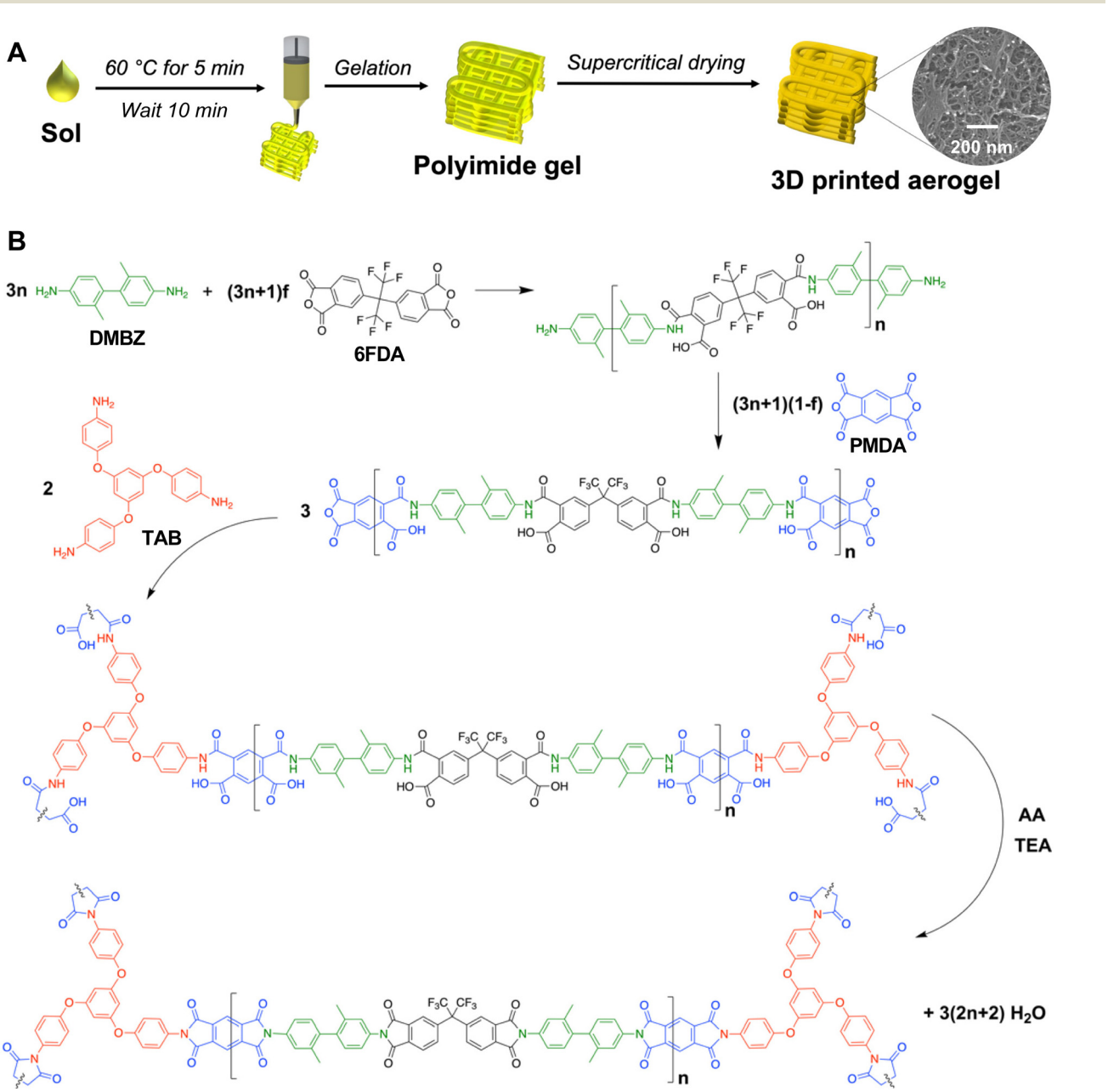

Fig. 1 (A) Strategy for DIW of polyimide aerogels. Mild heating of the sol speeds gelation to produce a 3D printable ink, as defined by rheological properties. (B) Synthetic scheme of polyimide aerogels used here (f = 0.25 and n = 60).

Experimental

Materials

2,2′-Dimethylbenzidine (DMBZ), 4,4′-hexafluoroisopropylidene di(phthalic anhydride) (6FDA), and pyromellitic dianhydride (PMDA) were obtained from Chriskev, Inc. Dianhydrides were dried at 125 °C at reduced pressure for 24 h before use. 1,3,5-Triaminophenoxybenzene (TAB) was obtained from Triton Systems. Triethylamine (TEA) and acetic anhydride (AA) were purchased from Sigma Aldrich. *N*-Methylpyrrolidinone (NMP) and acetone were purchased from Fisher Scientific. Li_6PS_5Cl (LPSC) (~1 μm) was purchased from NEI Corporation, and polytetrafluoroethylene (PTFE, 675 μm) was purchased from Sigma Aldrich. Unless otherwise specified, all materials were used as received.

Instrumentation

Rheological properties were analyzed using an Anton Parr MCR 302 rheometer with a 25 mm parallel plate. 3D printing was performed on a Hyrel 3D Engine SR with an SDS-10 syringe extrusion head. Supercritical fluid extraction was performed with a fully automated (Wonderware software) multichamber high-pressure system (Accudyne Industries, LLC) using liquid CO_2. Nitrogen-adsorption porosimetry was carried out with an ASAP 2000 surface area/pore distribution analyzer (Micrometrics Instrument Corp.). Bulk densities were determined from the weight and the physical dimensions of the samples. A Micrometrics Accupyc 1340 helium pycnometer was used to measure the skeletal density of the specimens. A TA model 2950 HiRes instrument was used to perform thermogravimetric analysis (TGA) in air from ambient temperature to 750 °C at a ramp rate of 10 °C min^{-1}. Infrared spectroscopy was performed using a JASCO Fourier transform infrared (FTIR) spectrometer, model FTIR-4600LE MidIR, with attenuated total reflectance (ZnSe/diamond). Scanning electron microscopy was performed using a Hitachi S-4700 field emission scanning electron microscope after sputter-coating the specimens with platinum. Compression testing was performed on an Instron 5943 Universal Testing System with a 1 kN load cell according to ASTM D695-10 (compression rate of 1 mm min^{-1}).[90] Dimensions of dry compression cylinders are listed in Table S1.† Thermal conductivities were measured using a Trident thermal conductivity instrument (C-Therm Technologies Ltd) equipped with a thermal chamber with a temperature control range of −50 to 200 °C. Thermal insulation performance was evaluated using a heating setup consisting of a power source (SmoTecQ, model 4336304932), variable resistor (Elenco Electronics Inc., model RS500), test lead set (Elenco-THI, model TL-16), heating plate (Zerodis, model Zerodis7i2r1quwgt-02), and infrared thermometer (Etekcity, Lasergrip 774). Electrochemical testing was performed on a Solartron Electrochemical Interface SI 1287 and Impedance Analyzer SI 1260. Digital images were recorded using an iPhone 11 Pro.

Aerogel synthesis

Synthesis was performed at ambient pressures and temperatures with atmospheric exposure in a ventilated hood according to a previously reported procedure;[55,91] the chemistry of the aerogel synthesis is shown in Fig. 1B. Reagent amounts were selected to yield a polymer concentration of 10 wt% and a chain length of n = 60. The fluorinated monomer 6FDA was incorporated to increase the flexibility of the aerogel,[47,48] and the 6FDA : PMDA molar ratio was 1 : 3. For example, DMBZ (1.1540 g, 5.436 mmol) was dissolved in NMP (16.89 mL) and stirred for 15 min until dissolved and the solution became translucent. Then, 6FDA (0.6138 g, 1.382 mmol) was added in small increments over a 10 min period. After stirring for 30 min to ensure complete dissolution, PMDA (0.9041 g, 4.145 mmol) was added and stirred for 10 min. To this solution, TAB (0.0241 g, 0.061 mmol) dissolved in NMP (5 mL) was added, then AA (4.18 mL, 44.250 mmol) was added. AA served as a water scavenger to promote the ring-closing condensation reaction, yielding the polyimide. After 10 min of stirring, TEA (0.770 mL, 5.526 mmol) was added to catalyze the crosslinking reaction, and the resulting sol was loaded into 10 mL syringes. For cast samples, the gel was allowed to form for 24 h in the syringe covered with Parafilm to prevent solvent evaporation, then subjected to solvent exchange as described below. For 3D printing, inks were prepared as follows.

Ink preparation

Inks were prepared by synthesizing the aerogel sol according to the above procedure in a 20 mL scintillation vial. After addition of TEA, the sol was mixed by vortex for 30 s, then the vial was immediately placed in a heated aluminum block at 60 °C and left undisturbed for 5 min. After 5 min, the sol was then transferred to 10 mL syringes for 3D printing and allowed to passively cool for 10 min.

3D part design

3D designs were created using Tinkercad.[92] Parts were designed to account for 15% linear shrinkage during the drying process and fit tolerances of the heating plate and battery. Cylinders 15 mm in diameter × 12 mm tall were designed for compression testing. A 3D model of a four-sided enclosure with dimensions shown in Fig. 2A was designed to fit around a heating plate with dimensions of 35.5 × 20.8 × 5 mm. Similarly, a 3D model of a casing was designed to surround a solid-state electrolyte coin cell battery in a holder as shown in Fig. 2B and C.

3D printing

Each ink-filled syringe was equipped with the desired nozzle size, either 27 Ga (0.21 mm inner diameter), 20 Ga (0.60 mm I.D.), or 16 Ga (1.19 mm I.D.). The syringe was placed on the extrusion cartridge of the 3D printer, and objects were printed onto a glass bed. Printing parameters are listed in Table 1. Images of the printing process and as-printed heating plate enclosure are provided in Fig. 3A and B.

Solvent exchange

The cast or printed structures were placed in a container covered with Parafilm to prevent solvent evaporation. After 24 h, the gels were extracted into a solution of 50 : 50 v/v NMP/

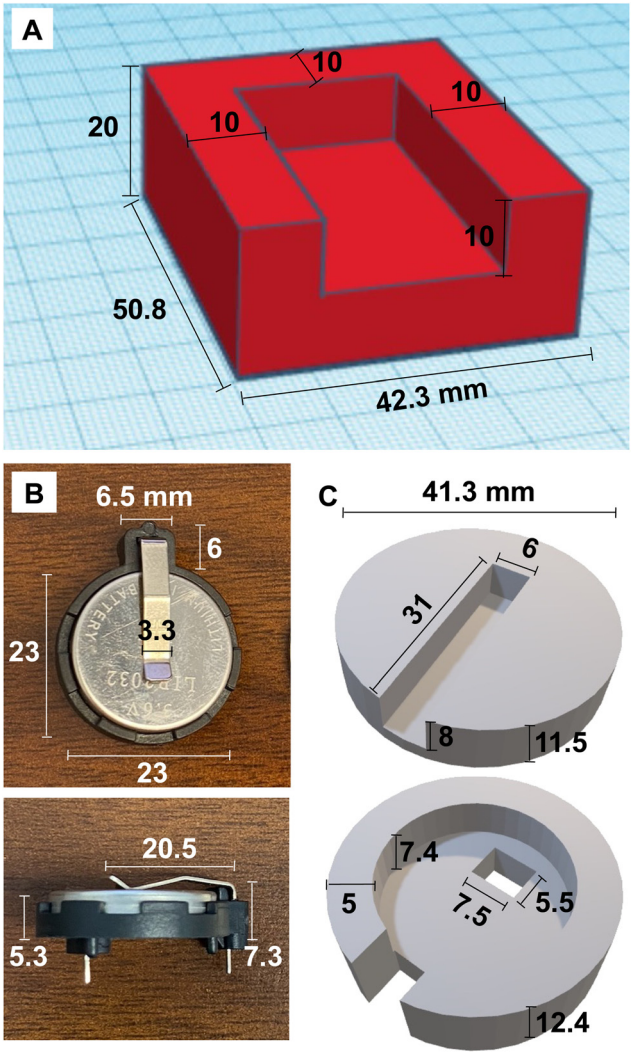

Fig. 2 (A) 3D model of heating plate enclosure. (B) Dimensions of coin cell battery holder. (C) 3D models of top and bottom of battery enclosure.

acetone and allowed to rest for 24 h. Then, the solvent was exchanged for acetone, and exchange of the acetone for fresh acetone was performed every 24 h, for a total of 5 solvent washes. The acetone-saturated gels were then transferred to an autoclave, submerged in acetone, and sealed in a supercritical fluid extraction vessel.

Supercritical fluid extraction

Gels were submerged in acetone while being loaded into a stainless-steel vessel with a 20.7 MPa per 100 °C rating. Once sealed, the vessel pressure was brought to 7 MPa at room temperature (25 °C) while the vessel was filled with liquid CO_2 using a pneumatic pump. The gels were soaked in liquid CO_2 for 30 min, then the contaminated CO_2 was drained at a rate of 9 g min^{-1} until the mass corresponding to a full vessel had been removed while exchanging for clean CO_2. This was repeated for 4 cycles. The temperature was then increased to 35 °C at a rate of 5 °C min^{-1} with a maximum pressure of 9 MPa to produce supercritical CO_2 (7.3 MPa, 32 °C). This supercritical step avoids crossing the CO_2 phase boundary, thus reducing the interfacial interaction between the solvent and polyimide. This inhibits pore collapse *via* surface tension or capillary force, enabling the structure to maintain its 3D integrity. Once the supercritical stage was reached, the system was vented to ambient pressure while maintaining a temperature of 35 °C, and the CO_2 within the aerogels was in the gas phase. The vessel was then opened to retrieve the aerogels, replacing the CO_2 in the structures with air and returning the samples to room temperature. Samples were dried under reduced pressure at 60 °C for 24 h to remove any residual solvent. The supercritically dried heating plate enclosure is displayed with measured dimensions in Fig. 3C.

Rheometry

All rheological experiments were performed using an Anton Parr MCR 302 rheometer with a 25 mm parallel plate at 25 °C, with a gap distance of 1 mm. Three samples of each type were run for each experiment. The untreated sol was directly loaded onto the rheometer for testing immediately after addition of TEA (the catalyst and final component) and vortex mixing for 30 s. The aged sol was allowed to sit undisturbed for 15 min before testing. For the ink, the sol was heated at 60 °C for 5 min immediately after vortex mixing, then allowed to sit undisturbed for 10 min before testing (*i.e.*, a total of 15 min had passed since the completion of the sol synthesis); of note, in the gel point experiment, testing of the ink began immediately after removal from the heat.

A strain amplitude sweep was performed on each sol and ink three times from 0.001 to 1000% strain at a frequency of 1 s^{-1}, and storage and loss moduli were measured. A shear rate ramp from 1 to 1000 s^{-1} was also performed on each sol and

Table 1 Printing parameters for various structures prepared herein

	Nozzle size (Ga mm^{-1})	Layer height (mm)	Extrusion rate (g min^{-1})	Printhead speed (mm s^{-1})	Infill (%)	Infill pattern
Lattice	14/1.60	1.5	0.6	10	20	Rectilinear
Lattice	20/0.60	0.6	0.3	10	20	Rectilinear
Lattice	27/0.21	0.2	0.1	10	20	Rectilinear
Compression cylinders	16/1.19	1.0	0.5	10	30	Concentric
Four-sided enclosure	16/1.19	1.0	0.5	10	50	Rectilinear
Battery casing	16/1.19	1.0	0.5	10	50	Rectilinear

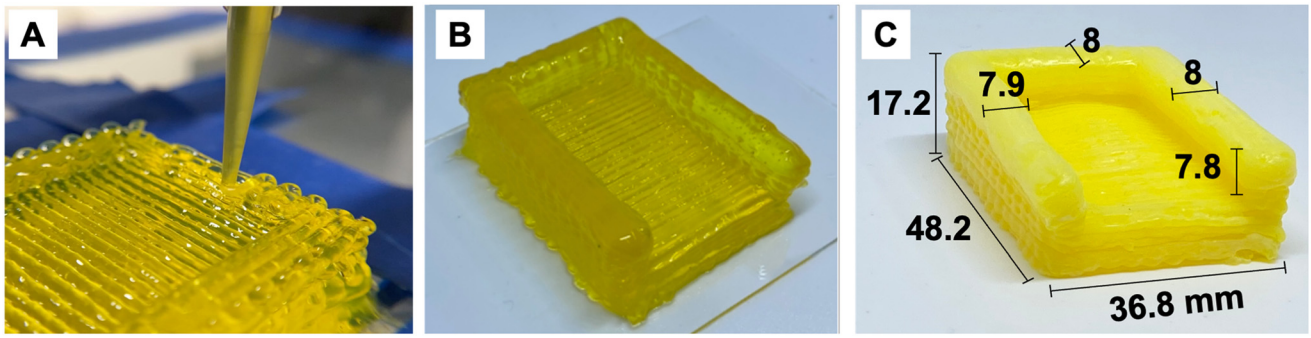

Fig. 3 (A) 3D printing of enclosure for heating plate. (B) As-printed enclosure before drying. (C) Printed and dried enclosure with measured dimensions.

ink, and viscosity was measured. A three-interval thixotropy test was performed by applying a strain of 0.1% at a shear rate of 0.1 s^{-1} for 2 min, then the shear rate was increased to 10 s^{-1} and held constant for 1 min, then decreased back to 0.1 s^{-1} and held constant for 2 min. The gel points of the sols were determined using small strain oscillation in the linear viscoelastic region. Specifically, samples were sheared at 0.1% strain at a frequency of 1 s^{-1} for 60 min to encompass the time range of gelation. The gel point was taken as the time at which the storage and loss moduli became equivalent.

Thermal conductivity

Thermal conductivities of the samples were measured using a C-Therm Trident according to the modified transient plane source method (ASTM D7984-21)[93] at temperatures ranging from −50 to 150 °C in 25 °C increments. Samples were held at the target temperature for 30 min to equilibrate, and three measurements were taken at each temperature.

Thermal insulation of heating plate

The thermal insulation capability of the printed aerogel was evaluated using a printed aerogel enclosure surrounding a heating plate, with one side of the heating plate left exposed. Temperature control was achieved using a variable resistor as shown in Fig. 4. As the temperature of the hotplate increased, temperatures of both the plate and the aerogel surface were measured using an infrared thermometer. After each change in resistance, the temperature was allowed to equilibrate for 5 min before measurements were recorded. Three measurements were taken in the center of each surface at each resistance setting. At the maximum heating plate temperature, temperature readings were also taken after 30, 60, 90, and 120 min.

Preparation of solid-state electrolyte battery

Solid-state electrolyte films were fabricated through a dry-processing technique. First, the lithium-ion conducting sulfide

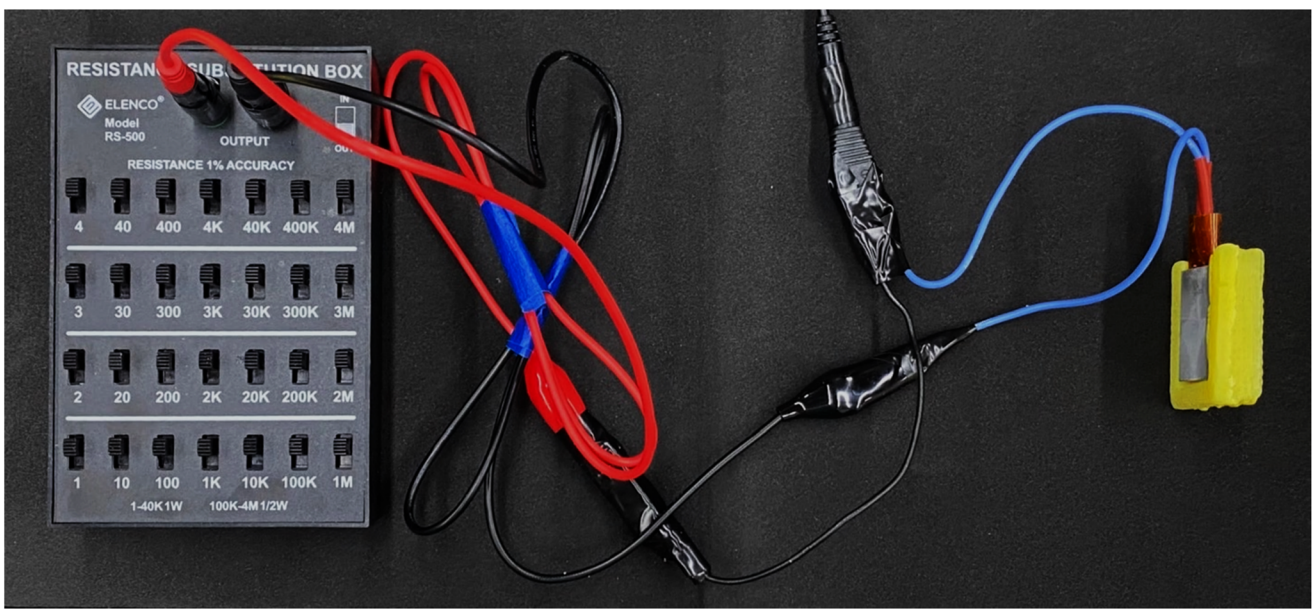

Fig. 4 Experimental setup with variable resistor controlling temperature of heating plate enclosed in aerogel.

powder (LPSC) was added to a mortar held above 80 °C on a hot plate in an argon-filled glovebox to maintain moisture and oxygen levels below 1 ppm. The powder was ground by hand with a pestle until large agglomerations were no longer visible, then a premeasured amount of powdered PTFE was added to the heated sample for a final mass ratio of 99 : 1. The LPSC–PTFE mixture was mechanically mixed by hand until a single platelet formed. The platelet was removed from the mortar and placed on a heated flat aluminum plate (80 °C) and rolled using a steel rod. This process was repeated after folding the thinning platelet several times until a robust freestanding film was obtained. The film was rolled to roughly 200 μm, and a circular sample 12.7 mm in diameter was punched from the film and placed between two graphite foils which served as current collectors. This three-layered assembly was placed into a steel pellet die and pressed at 380 MPa for approximately 10 min to ensure adequate compaction of the sulfide particles within the film. Finally, the assembly was placed inside a CR2032 coin cell and crimped at 210 kPa to allow removal from the glovebox for electrochemical testing.

Electrochemical testing

The assembled coin cell was placed in a coin cell holder to allow proper current collection and lead attachment before electrochemical testing. 10 mV amplitude was applied across the cell under a frequency sweep from 100 000 to 1 Hz. The coin cell was tested under three conditions: (1) as fabricated at room temperature, (2) after preheating to 80 °C then removed to ambient conditions without thermal insulation, and (3) after preheating to 80 °C and removed to ambient conditions while enclosed in aerogel casing. Testing was started approximately 5 min after removal from the heat source, and resistance was measured over 100 min. Ionic conductivities (σ) were calculated using the equation $\sigma = l/RA$ where l is the cross-section thickness of the film, R is the obtained resistance, and A is the area of contact between the film and the attached current collectors.

Results and discussion

The polyimide sol was synthesized as described above. To achieve the rheological requirements of DIW printing, namely, yielding, high viscosity, shear-thinning, and thixotropy, the gelation process was promoted through a mild heat treatment of the sol. This heat treatment increased the rate of the polymerization and crosslinking reactions, resulting in decreased gelation time. Heat treatment temperatures (50, 60, 80 °C) and timespans (2, 5, 10 min) were screened to achieve facile printability. Heating the ink to 60 °C for 5 min enhanced gelation without fully imidizing the structure, which would yield an unprintable gelled network. To identify the effects of heat treatment on the gelation process, FTIR spectra were collected at various times throughout the gelation of unheated and heated sol up to 60 min as shown in Fig. S1.† The sample at 0 min of reaction time is the same for both untreated and heated sols. The intensity of the peak corresponding to the imide C=O stretching (1724 cm^{-1}) relative to the intensity of the peak corresponding to the C–F bond (1172 cm^{-1})[94,95] is compared in Fig. S2.† These data indicate that heat treatment facilitates polymerization and crosslinking in the initial time-points of measurement, thus reducing gelation time, thickening the sol, and expediting printability. For DIW printing, after heat treatment, allowing the ink to cool to ambient temperature over 10 min enabled printing across a timespan of approximately 30 min. Furthermore, the 10 min cooling window provides time to load the ink into a syringe.

The printability of the sol ink was determined by attempting to extrude it from a variety of nozzle sizes, then evaluating whether extrusion was possible, along with identifying defects in the printed structures such as slumping or undesired voids. Larger nozzles enable high-throughput printing, since the filaments have larger diameters and larger layer heights may be used to minimize print time. In complement, smaller nozzles are ideal for achieving fine details for high-resolution printing. As shown in Fig. 5, the ink was found to be printable using nozzles with a wide range of inner diameters (1.60 to 0.21 mm). The printed structures were stable and resisted slumping and spreading regardless of nozzle size, indicating that the ink rheology was successfully modified by the heat treatment process to enable DIW printing.

Parallel plate rheometry was performed to quantify the behavior of the sol over time with and without heat treatment. Three sample types were evaluated – one immediately after catalyst addition (untreated sol), one 15 min after catalyst addition (aged sol), and one heated for 5 min and aged for 10 min (ink). Since the factors of printability primarily arise from the yielding process, yielding behavior was evaluated using a strain amplitude sweep from 0.01 to 1000% strain. The storage and loss moduli (G' and G'', respectively) for untreated sol, aged sol, and ink are plotted in Fig. 6A and S3.† As expected, the untreated and aged sols exhibited linear viscoelastic behavior throughout the experiment, with $G'' > G'$ indicating that viscous behavior dominated their responses to shear, and they remained liquidous. As such, the sols flowed readily and were not printable. The impact of gelation was also observed with the stable value of G' increasing by over four orders of magnitude with 15 min of aging, indicating increased energy storage within the sol over time after catalyst addition. In contrast, for the ink, $G' > G''$ at low strain amplitudes, but above 105% strain, G'' became larger than G', indicating that the viscous response dominated the material behavior, and the ink flowed. Therefore, only the ink is a yielding fluid, which demonstrates that heat treatment endows printability of polyimide sol by imparting solid-like behavior at low strain amplitudes and enabling flow at large strain amplitudes.

The viscosities of the untreated sol, aged sol, and ink were measured throughout a shear rate sweep from 1 to 1000 s^{-1}. This experiment allows for the observation of shear-rate dependence of viscosity, particularly any shear-thinning performance, which is necessary for DIW. A successful ink should have

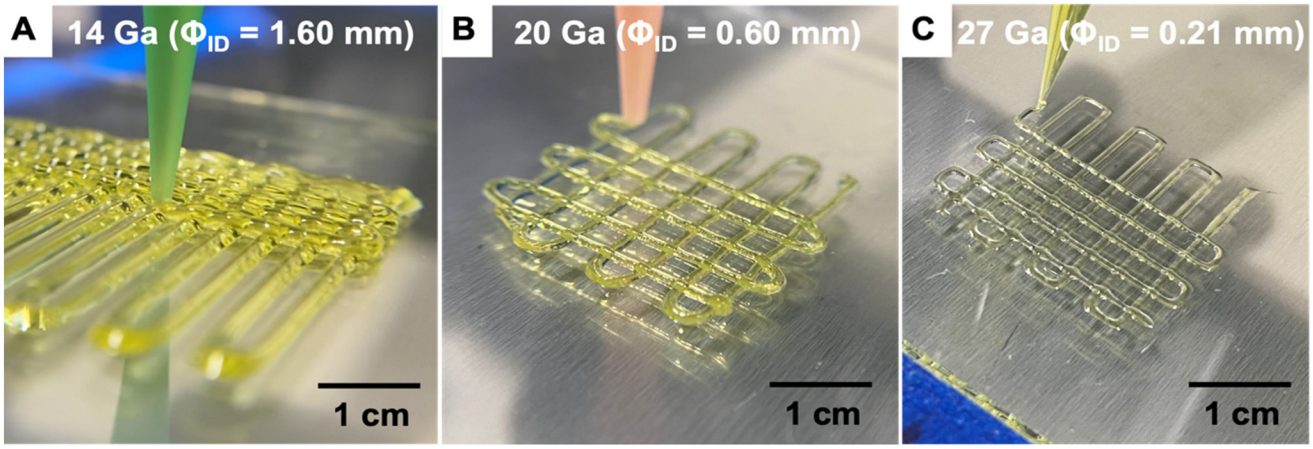

Fig. 5 Photographs showing direct ink writing of aerogel lattices using different nozzle sizes (A) 14 Ga, (B) 20 Ga, (C) 27 Ga.

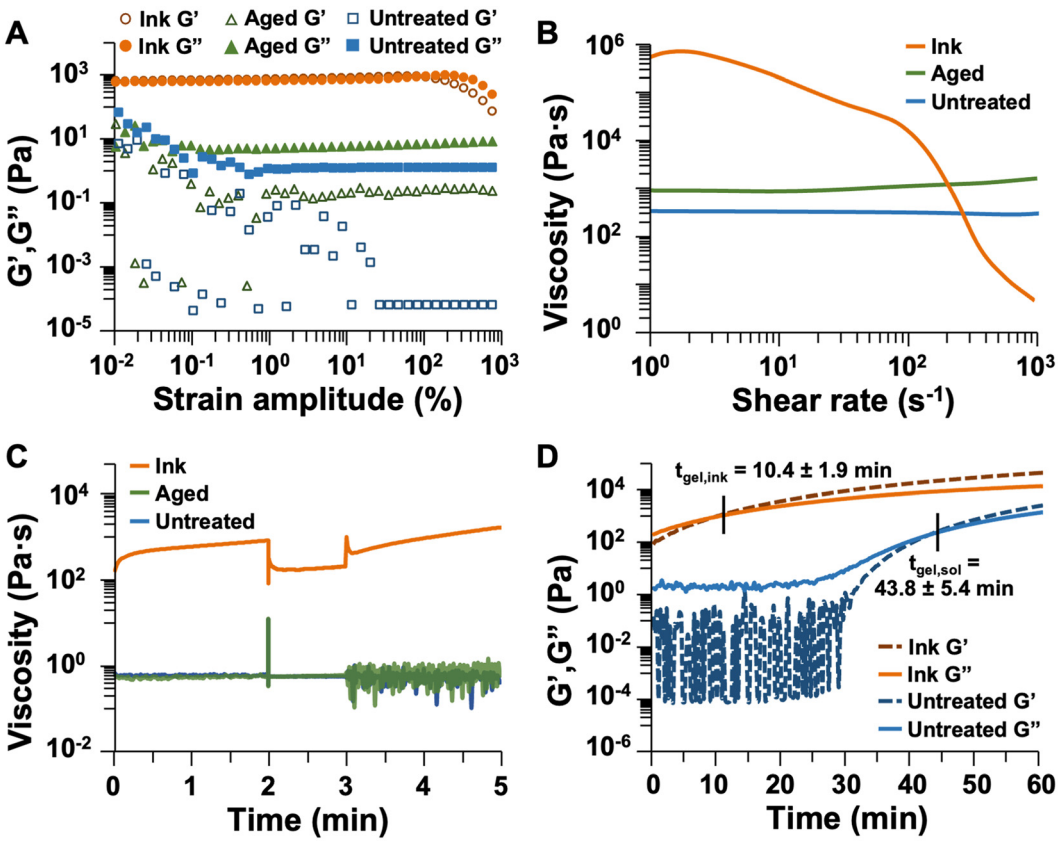

Fig. 6 Rheological studies of untreated sol, aged sol, and ink. (A) Storage and loss moduli *vs.* strain amplitude. (B) Viscosity *vs.* shear rate. (C) Viscosity *vs.* time during three-interval thixotropy test. (D) Storage and loss modulus *vs.* time during gel point measurement for untreated sol and ink.

a high viscosity at low shear rates (usually between 10^2 and 10^6 mPa s when measured at 0.1 s^{-1}).[74–76,79] As shown in Fig. 6B and S4,† the untreated sol exhibited minimal shear-thinning behavior, with a viscosity of 316 mPa s at a shear rate of 1 s^{-1} decreasing to 280 mPa s at a shear rate of 1000 s^{-1}. At shear rates below 1 s^{-1}, the sol exhibited unstable viscosity values. Aging the sol for 15 min resulted in a higher viscosity of 838 mPa s at a shear rate of 1 s^{-1} and slight shear-thickening behavior, with the viscosity increasing to 1493 mPa s at a shear rate of 1000 s^{-1}. This unexpected behavior (apparent shear thickening, rather than shear thinning) is likely due to ongoing gelation of the sample during the measurement; thus,

the aged sol would not possess the degree of intermolecular interactions necessary to produce shear-thinning behavior but rather forms aggregates of oligomers upon shearing. In contrast, heating the sol to produce an ink facilitates gelation and formation of a network which reversibly breaks down upon the application of shear. This explains the high initial viscosity (448 000 mPa s at a shear rate of 1 s^{-1}) and large degree of shear-thinning behavior (viscosity decreased to 632 mPa s at a shear rate of 1000 s^{-1}) observed for the ink. These factors are necessary for DIW printing, and the measured viscosities quantify the impact of heating to make the sol printable.

Thixotropy is another factor which is important for DIW. An ink should have a relatively high viscosity which decreases rapidly upon the application of shear, then recovers to its initial value once the shear is stopped. To simulate the extrusion process from a DIW printer, a three-interval thixotropy test (3ITT) was performed. In this experiment, a low shear rate (0.1 s^{-1}) was applied for 2 min to simulate the material in the syringe prior to extrusion (in reality, the shear rate is 0 s^{-1} in this scenario, but a small shear must be applied to obtain measurements in rheology). Then, the shear rate was rapidly increased to 10 s^{-1} and held constant for 1 min to simulate extrusion from a DIW nozzle, followed by decrease of the shear rate to 0.1 s^{-1} to simulate the deposited material. Results for the three samples are plotted in Fig. 6C and S5.† The average viscosities for each sample in the three intervals are provided in Table 2. The untreated and aged sols had similar viscosity values throughout the experiment. In contrast, heating imparted thixotropic performance with the ink exhibiting a clear decrease in apparent viscosity with increased shear rate, then recovery of initial viscosity in the third interval. Throughout this experiment, an increase in viscosity was observed for the ink, particularly in the low-shear rate intervals, which is attributable to increasing viscosity during the continued polymerization of the sol. This also contributed to the larger standard deviation in ink viscosity. Based on the large magnitude of the viscosity change between intervals, this performance can be isolated from the gelation process to indicate that the ink is thixotropic.

The working time of the ink can be related to the gelation time. The gelation time of untreated sol was measured and compared to that of the ink (*i.e.*, heated sol) using constant small strain oscillation over time, with results plotted in Fig. 6D and S6.† From this experiment, G' and G'' were measured at a constant strain amplitude of 0.1%, and the gelation time was noted as the point at which $G' = G''$ (*i.e.*, when solid-like behavior dominated the sample). For the untreated sol, the average gelation time was 44 min. In contrast, heating the sample at 60 °C for 5 min reduced the gelation time to 10 min and enabled printing by DIW. Notably, the working time of the ink ranges between approximately 15 and 45 min after removal from the heating source, after which the ink solidifies to an extent that it cannot form a smooth extruded filament. This qualitative information indicates that quantitative measures of gelation time do not fully encompass printability. Apparent gelation under experimental conditions does not preclude an ink from being printed, since the pressure applied by a DIW printer, and therefore the shear to which the ink is subjected, can be modulated to influence the apparent rheology of the ink. Therefore, this gel point measurement provides a relative indication of how quickly an ink might become printable.

Table 2 Average viscosities of untreated sol, aged sol, and ink in each interval of the 3ITT (n = 3)

	Avg. viscosity, interval 1 (mPa s)	Avg. viscosity, interval 2 (mPa s)	Avg. viscosity, interval 3 (mPa s)
Untreated sol	590 ± 21	555 ± 6	532 ± 167
Aged sol	522 ± 31	552 ± 12	629 ± 297
Ink	603 000 ± 152 000	189 000 ± 15 600	993 000 ± 375 000

To ensure full gelation, printed or cast structures were covered to prevent solvent evaporation and allowed to rest for 24 h before extracting into 50 : 50 v/v NMP/acetone, which was exchanged for acetone over the course of 5 solvent washes as previously described. The gels could then be dried by supercritical fluid extraction to yield highly porous aerogels.

The properties of the dry printed and cast aerogels were compared to identify the influence of printing on the material performance. Cast samples were molded in 10 mL syringes, whereas inks were printed to form cylinders 10 mm tall × 12 mm in diameter. The chemical composition of the cast and printed dry aerogels were probed by Fourier transform infrared (FTIR) spectroscopy with attenuated total reflectance. The spectra shown in Fig. 7A highlight that regardless of processing, all aerogels bear stretching frequencies corresponding to the polyimide structure.[4,49] Namely, both spectra show the imide ring deformation peak at 724 cm^{-1}, aromatic peaks at 816 and 1100 cm^{-1}, the imide C–N peak at 1362 cm^{-1}, and the imide C=O peak at 1718 cm^{-1}. Based on the FTIR spectra, the heat treating and printing processes do not significantly influence the chemical structure of the resulting aerogel. Thermogravimetric analysis (TGA) was performed to evaluate the thermal stability of both the cast and printed aerogel species. Sample weights and first derivatives of the weight loss profiles are plotted in Fig. 7B, measured from ambient temperature to 750 °C. No significant weight loss up to 450 °C was observed for both samples, which indicates complete imidization (incomplete imidization would result in a mass loss around 200 °C with expulsion of water).[50] The temperature of 5% weight loss ($T_{d5\%}$) is approximately 500 °C in both samples, with full decomposition around 720 °C. The polyimide exhibits a two-stage decomposition consistent between printed and cast samples. These results demonstrate that processing does not impact thermal stability of the aerogel, and that the materials have promise for high-temperature applications, such as insulating electronic components to prevent heat transfer.

A key component to aerogel function is their nanoscale porous structure, which is produced from solvent removal without collapsing the solid polymer network; this imparts low bulk density, high porosity, and high surface area. Bulk den-

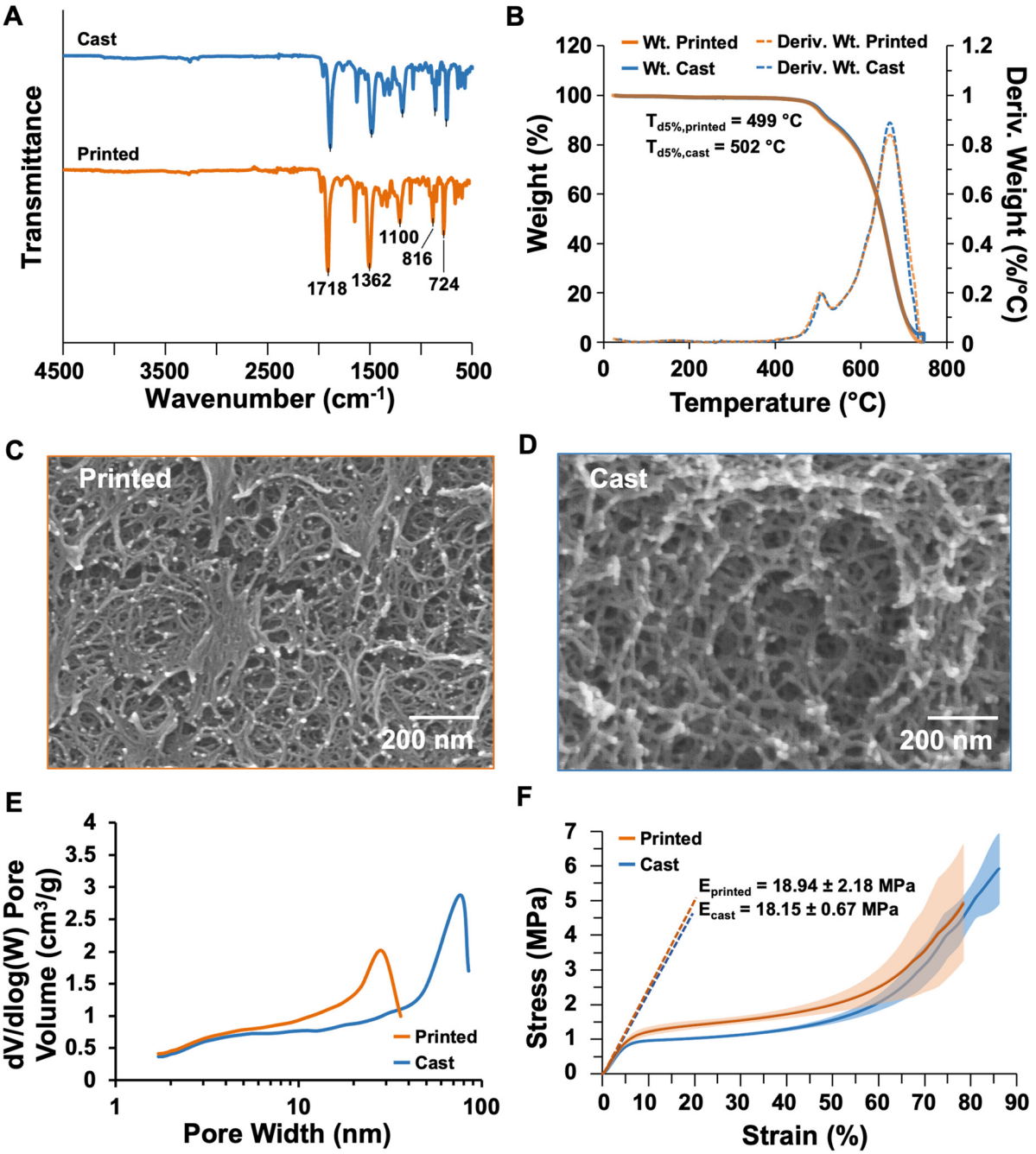

Fig. 7 Characterization of cast and printed aerogels. (A) FTIR-ATR spectra. (B) Thermal weight loss profiles and first derivatives. (C) Scanning electron micrograph of fractured surface of printed sample. (D) Scanning electron micrograph of fractured surface of cast sample. (E) Pore size distributions. (F) Compression stress–strain profiles. Shaded areas indicate standard deviation (n = 3).

sities of cast and printed samples were calculated from measured masses and dimensions of compression cylinders. Tables 3 and S1† indicate that heat treatment and printing only slightly impact bulk density, as the cast aerogel had a bulk density of 0.109 ± 0.0003 g cm^{-3}, whereas the printed aerogel had a bulk density of 0.100 ± 0.004 g cm^{-3}. The slight difference in bulk density between the two sample types may result from small discontinuities in the material network as a result of the extrusion process, which could contribute to the presence of more void space in the printed sample. The skeletal density, that is, the density of the polyimide network without porosity, was measured by helium pycnometry and found to be approximately 1.3 g cm^{-3} in the cast sample and 1.5 g cm^{-3} in the printed sample. Plotted results from the 50 cycles of the experiments are provided in Fig. S7.† From the bulk and skeletal densities, the volume of each sample occupied by air, *i.e.*, porosity, was calculated. The cast aerogel had a porosity of 91.5%, whereas the printed aerogel had a slightly

Table 3 Physical properties of cast and printed aerogels

	Bulk density (g cm^{-3})[a]	Skeletal density (g cm^{-3})[b]	Porosity (%)	Linear shrinkage (%)[a]	Surface area (m^2 g^{-1})	Onset of decomp. (°C)	Compressive modulus (MPa)[c]
Cast	0.109 ± 0.0003	1.279 ± 0.053	91.5	11.93 ± 0.21	643.7	502	18.15 ± 0.67
Printed	0.100 ± 0.004	1.349 ± 0.105	92.6	14.51 ± 3.58	777.1	499	18.94 ± 2.18

[a] Standard deviations were calculated from $n = 5$ samples. [b] $n = 50$ cycles on the same sample. [c] $n = 3$ samples.

higher porosity at 92.6%. Like the difference in bulk density between the two sample types, this change in porosity may be attributed to voids formed the extrusion process. Both sample types provide a high volume of air favorable for thermal insulation performance. The linear shrinkage of the aerogels was also measured by comparing the diameter of the dried gel with that of the mold or printed geometry. The cast aerogels experienced a linear shrinkage of approximately 12%, whereas the printed shrunk approximately 15%. Although the printed structures appear to have shrunk more based on these values, the larger standard deviation (3.6%, $n = 5$) indicates that the diameter measurements may be influenced by slight variations due to the nature of the extrusion-based printing process. This linear shrinkage must be accounted for when designing molds or computer-aided design files for 3D printing, as in our thermally insulating enclosures discussed below.

The scanning electron micrographs in Fig. 7C, D, and S8† elucidate that smaller, more compact tendril-like structures formed in the printed aerogel compared to the cast sample. This morphology may result from compressive forces during the printing process. Since the viscous sol is close to gelation when extruded, the pressure of extrusion may cause slight pore collapse with minimal impact on the properties of the resulting structure. The surface areas and pore size distributions of the aerogels were determined using gas adsorption analysis according to Brunauer–Emmett–Teller (BET) theory. Pore size distributions are plotted in Fig. 7E, and adsorption–desorption curves are plotted in Fig. S9.† Most of the pores of the printed aerogel were approximately 20 nm in diameter, whereas the cast aerogel had larger pores approximately 70 nm in diameter. This finding also corresponds to a higher surface area for the printed sample (777 m^2 g^{-1}, Table 3) compared to the cast sample (644 m^2 g^{-1}). The increased surface area of the printed aerogel could improve the performance of such materials in applications like catalyst support structures, for instance.

To evaluate performance-related mechanical properties, cast and printed cylinders were compressed according to ASTM D695-10.[90] Stress–strain profiles are plotted in Fig. 7F and S10.† Both aerogel samples exhibited a similar compressive response, with a linear elastic region up to approximately 4% strain and yield up to approximately 60% strain. After this point, both aerogels also exhibited densification and elastic hardening which is typical of these materials.[82] No fracture was observed, so the experiment was ended when the aerogel was compressed from an initial height of approximately 1 cm (see Table S1†) to a height of 1 mm. The compressive moduli were calculated using the slope between 2 and 4% strain for both materials. As reported in Table 3 and plotted in Fig. 7F, the cast aerogel had a compressive modulus of 18.15 ± 0.67 MPa ($n = 3$), which is in line with other polyimide aerogels synthesized using the same crosslinking procedure.[5] The printed aerogel had a similar modulus of 18.94 MPa, indicating that this DIW process could produce aerogel structures which can withstand the stresses of high-demand applications. The printed structures exhibited higher variability between results, with a standard deviation of 2.18 MPa. This variability may be attributed to artifacts of the DIW process within the printed shape, such as visible layers, divots between layers, curved edges, and slight dimensional variations, as seen in Fig. S10C.† These features are common to DIW but can be mitigated by using smaller nozzles to achieve finer resolution and/or by printing more slowly to facilitate material solidification before printing subsequent layers. Both of these approaches increase printing time, but future standardization in DIW materials development and print processes are expected to facilitate increased efficiency and higher quality prints across materials systems.

The thermal conductivities of cast and printed samples were measured at temperatures ranging from −50 to 150 °C as plotted in Fig. 8A, with full data provided in Table S2.† Both sample types exhibit low thermal conductivities across this temperature range (<50 mW m^{-1} K^{-1}),[96] which demonstrates that both cast and printed aerogels are excellent thermal insulators. The thermal insulation performance of the printed aerogel was evaluated by an experiment imitating a battery cell undergoing thermal runaway. First, a four-sided enclosure designed to fit around a heating plate was 3D printed and supercritically dried (Fig. 2A and 3). The printed structure maintained its shape throughout drying and successfully enclosed the heating plate. The heating plate was controlled by a variable resistor as shown in Fig. 4. As the resistance was decreased (*i.e.*, temperature of the heating plate increased), both the temperature of the plate and the aerogel were measured using an infrared thermometer (temperature equilibrated for 5 min at each step). Results at different temperatures are reported in Table S3† and demonstrate that the aerogel surface maintained ambient temperature (approximately 26 °C), even when the heating plate reached the maximum temperature of approximately 120 °C. When the heating plate was held at 120 °C (Fig. 8B and Table S4†), the aerogel surface temperature reached approximately 30 °C in

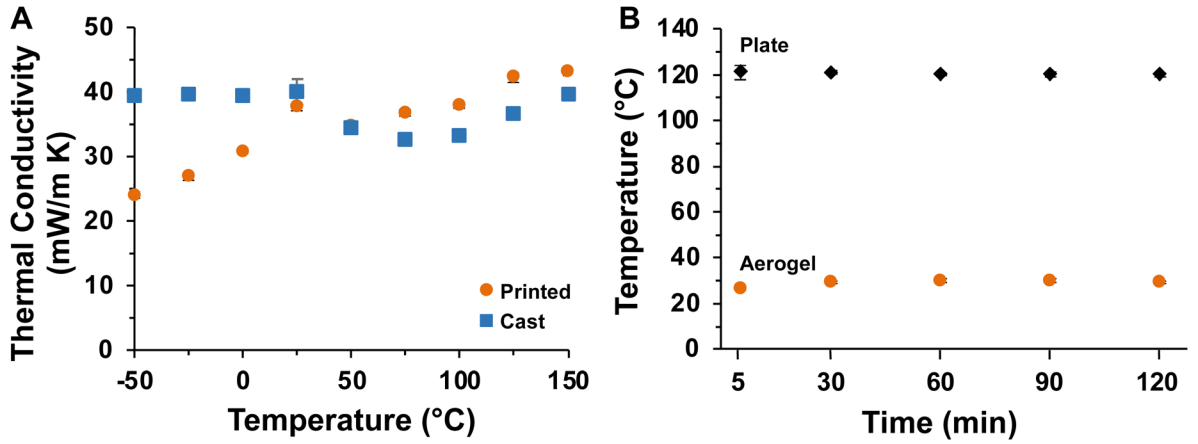

Fig. 8 (A) Thermal conductivity of cast and printed aerogels at various temperatures. (B) Temperature of plate and aerogel over time. Error bars indicate standard deviation (n = 3).

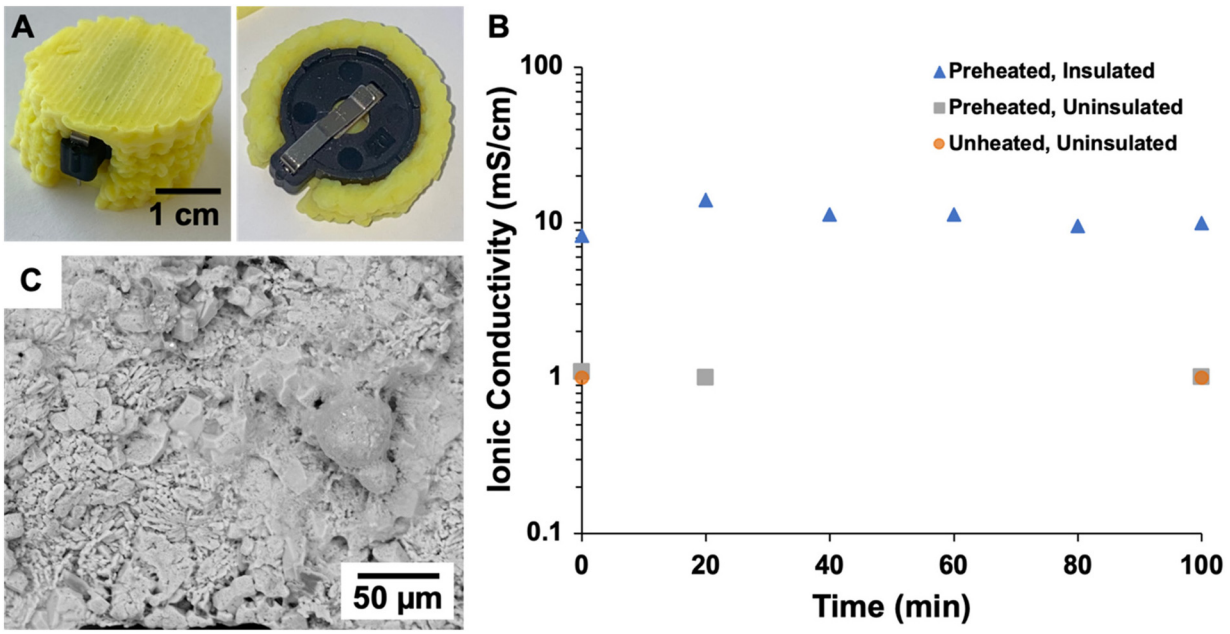

Fig. 9 (A) 3D printed aerogel casing for coin cell battery. (B) Ionic conductivity evaluation across 100 minutes for uninsulated battery without preheating, after preheating to 80 °C and removed to ambient air, and with aerogel insulation and after preheating to 80 °C and removed to ambient air. (C) Scanning electron micrograph of the cross-section of the LPSC:PTFE film after electrochemical measurements.

60 min and showed no increase after 90 and 120 min of test time. These results indicate the potential of 3D printed aerogels for thermal insulation applications.

In addition to the thermal monitoring verification, an electrochemical test was designed to investigate the impact of 3D printed polyimide aerogel thermal insulation on the ionic conductivity of a solid-state electrolyte coin cell battery. LPSC:PTFE films were prepared and assembled within a coin cell, which was placed in a coin cell holder for electrochemical testing. The ionic conductivity of the battery was evaluated with no heat treatment and no insulation, after preheating to 80 °C and with no insulation, and after preheating to 80 °C and encased in an aerogel enclosure. Fig. 9A displays the 3D printed aerogel casing surrounding the coin cell holder, and the coin cell and holder and 3D models are displayed in Fig. 2B and C, respectively. As illustrated in Fig. 9B, the uninsulated LPSC:PTFE film achieved an ionic conductivity of 1 mS cm^{-1} and demonstrated little change at over time, regardless of preheating, whereas the insulated cell showed an impressive increase in ionic conductivity to 14 mS cm^{-1} at 20 min of test time. Furthermore, the ionic conductivity was maintained at approximately 10 mS cm^{-1} for at least 100 min. After testing, the morphology of the LPSC:PTFE film was evaluated using scanning electron microscopy (Fig. 9C), which demonstrates a

homogeneous distribution of the electrolyte components with no visible layers nor thermal damage. Solid-state electrolyte batteries offer a unique tolerance to high temperatures which can be paired with thermal insulation to increase ionic conductivity. 3D printed polyimide aerogels have potential for use in creating custom-fit insulating structures for batteries and other electronic components with complex geometries.

Conclusions

Herein, we report a new approach to 3D printing polyimide aerogels using the facile, cost-effective process of direct ink writing (DIW), without requiring particle fillers, extreme conditions, or additional post-processing steps. Mild heat treatment of a sol promoted gelation, decreased processing time, and achieved the required rheology for printing. Rheological studies indicate that the required properties of yielding, high viscosity, shear-thinning behavior, and thixotropy were not present in the untreated sol, but heat treatment imparted this performance. Printability testing elucidated that the sol ink was printable through a wide range of nozzle sizes, from 0.21 to 1.60 mm inner diameter. This is integral to achieving high-resolution printing with smaller nozzles and high-throughput printing with larger nozzles. After supercritical drying, we illustrate minimal differences in the chemical, thermal, and mechanical properties of the printed aerogel compared to the cast aerogel, with the printed sample having a slightly lower bulk density, slightly higher porosity, lower average pore size, and much greater surface area, which are attributed to the slightly smaller polymer struts in the printed gel. Thermogravimetric analysis indicated that both aerogels were stable up to approximately 500 °C, demonstrating their usefulness in thermal insulation applications. Furthermore, the aerogels had comparable mechanical performance, with similar compressive moduli of 18.1 MPa for the cast gels and 18.9 MPa for the printed gels. Key properties of the pure aerogel are maintained even after heat treating and 3D printing.

The performance of the printed aerogel for thermal insulation was evaluated by placing a heating plate in a printed aerogel enclosure. The printed aerogel exhibited a remarkable ability to prevent heat transfer, maintaining room temperature on the exterior aerogel surface approximately 8 mm from the heating plate, even as the plate reached 120 °C. The thermal insulation capabilities were confirmed through additional testing of the ionic conductivity of a solid-state electrolyte coin cell battery over time after preheating. A bespoke printed polyimide aerogel casing offered sufficient thermal insulation to increase the battery ionic conductivity tenfold over at least 100 min. Evaluation of the application-based performance of the printed aerogels is ongoing, particularly at higher temperatures as the aerogel is stable up to 500 °C. The facile method for 3D printing aerogels reported herein opens exciting opportunities across the class of sol–gel-derived materials to move beyond the geometric limitations of molding. In the future, print process modifications could mitigate working time considerations. For example, a printer equipped with inline heating and cooling could impart the necessary rheology for direct ink writing while allowing for a continuous stream of feedstock sol, rather than having to exchange syringes midprint. Industrial processes could increase the amount of ink that could be prepared at once, so long as ideal heat treatment conditions are identified. This will broaden access to complex structures made from pure aerogel for thermal insulation of electronic components, acoustic impedance, catalyst supports, and beyond.

Nomenclature

3D	Three-dimensional
DIW	Direct ink writing
DMBZ	2,2′-Dimethylbenzidine
6FDA	4,4′-Hexafluoroisopropylidene di(phthalic anhydride)
PMDA	Pyromellitic dianhydride
TAB	1,3,5-Triaminophenoxybenzene
TEA	Triethylamine
AA	Acetic anhydride
NMP	*N*-Methylpyrrolidinone
LPSC	Li_6PS_5Cl, lithium-ion conducting sulfide powder
PTFE	Polytetrafluoroethylene
TGA	Thermogravimetric analysis
FTIR	Fourier transform infrared
σ	Ionic conductivity
l	Cross-section thickness of solid-state electrolyte film
R	Measured resistance
A	Contact area between film and current collectors
G'	Storage modulus
G''	Loss modulus
3ITT	Three-interval thixotropy test
$T_{d5\%}$	Temperature of 5% weight loss
BET	Brunauer–Emmett–Teller

Author contributions

C.E.C., S.L.V., and E.B.P. conceived the research. S.L.V. provided the aerogel formulations. C.E.C. developed the 3D printing methodology, manufactured specimens, and performed FTIR measurements, rheometry, 3D printing, mechanical testing, thermal conductivity measurements, and heating plate insulation experiment. D.A.D. and C.E.C. designed the battery insulation experiment, D.A.D. produced the battery, and D.A.D. performed the electrochemical measurements. C.E.C., D.A.D., S.L.V., and E.B.P. analyzed data and interpreted results. C.E.C. made all figures. C.E.C. prepared the original draft, and all authors reviewed and edited. S.L.V. and E.B.P. supervised, administrated, and acquired funding for the research.

Conflicts of interest

There are no conflicts to declare.

Acknowledgements

The authors thank Dan Scheiman (Ohio Aerospace Institute) for thermal analysis and pycnometry measurements, Haiquan Guo (Ohio Aerospace Institute) for supercritical drying assistance and nitrogen sorption measurements, and Linda McCorkle (NASA Glenn Research Center) for taking scanning electron microscopy images. Dr Yifei Wang (Department of Materials Science and Engineering, Texas A&M University) is acknowledged for training on the heating element setup for preliminary experiments, and Dr Sadeq Malakooti (NASA Glenn Research Center) is acknowledged for training on thermal conductivity measurements. Ariel Tokarz (NASA Glenn Research Center) and Theresa Nosel (NASA Glenn Research Center) are acknowledged for assistance with 3D printing. The authors thank Dr Micah Green (Department of Chemical Engineering, Texas A&M University) and Kailash Arole (Department of Materials Science and Engineering, Texas A&M University) for consultation on supercritical drying. Krista Schoonover (Department of Chemistry, Texas A&M University) is acknowledged for assistance with analyzing FTIR data. The authors thank Dr Matt Pharr (Department of Mechanical Engineering, Texas A&M University), Jungho Shin (Department of Mechanical Engineering, Texas A&M University), and Victor Balcorta (Department of Materials Science and Engineering, Texas A&M University) for assistance with mechanical testing and Dr Chandler Benjamin (Department of Mechanical Engineering, Texas A&M University) for rheometry. Jessica Cashman (NASA Glenn Research Center) is acknowledged for initial discussions on applications of 3D printed aerogels. Dereck Johnson (NASA Glenn Research Center), Nicholas Starvaggi (Department of Chemistry, Texas A&M University), and Dr Peiran Wei (Soft Matter Facility, Texas A&M University) are acknowledged for initial discussions and assistance with preliminary experiments. The authors thank Nicholas Starvaggi and Chia-Min Hsieh (Department of Chemistry, Texas A&M University) for providing feedback on the manuscript draft. This work was funded by NSF DMR (Grant No. 2103182) and the Texas A&M University College of Engineering and College of Arts and Sciences. C. E. C. is supported by a NASA Space Technology Graduate Research Opportunity.

References

1 P. R. Aravind, P. Shajesh, G. D. Soraru and K. G. K. Warrier, *J. Sol-Gel Sci. Technol.*, 2010, **54**, 105–117.
2 *Aerogels Handbook*, ed. N. Leventis and M. M. Koebel, Springer Science+Business Media, 2011.
3 S. Ghaffari-Mosanenzadeh, O. Aghababaei Tafreshi, S. Karamikamkar, Z. Saadatnia, E. Rad, M. Meysami and H. E. Naguib, *Adv. Colloid Interface Sci.*, 2022, **304**, 102646.
4 S. Malakooti, S. L. Vivod, M. Pereira, C. R. Ruggeri, D. M. Revilock, R. Zhang, H. Guo, D. A. Scheiman, L. S. McCorkle and H. Lu, *Sci. Rep.*, 2022, **12**, 13933.
5 M. A. B. Meador, E. J. Malow, R. Silva, S. Wright, D. Quade, S. L. Vivod, H. Guo, J. Guo and M. Cakmak, *ACS Appl. Mater. Interfaces*, 2012, **4**, 536–544.
6 S. Kistler, *Nature*, 1931, **127**, 741.
7 Y. Deng, Y. Pan, C. Li, Z. Zhang, L. Gong, Y. Fu, L. Shi, H. Zhang and X. Cheng, *J. Energy Storage*, 2022, **56**, 106100.
8 S. Malakooti, H. G. Churu, A. Lee, T. Xu, H. Luo, N. Xiang, C. Sotiriou-Leventis, N. Leventis and H. Lu, *J. Non-Cryst. Solids*, 2017, **476**, 36–45.
9 T. Budtova, T. Lokki, S. Malakooti, A. Rege, H. Lu, B. Milow, J. Vapaavuori and S. L. Vivod, *Adv. Eng. Mater.*, 2023, **25**, 2201137.
10 S. S. Mirmoeini, M. Moradi, H. Tajik, H. Almasi and F. M. Gama, *Food Chem.*, 2023, **425**, 136493.
11 E. Gasmen, J. Marchetta and F. Sabri, *J. Packag. Technol. Res.*, 2023, **7**, 43–53.
12 L. Manzocco, K. S. Mikkonen and C. A. García-González, *Food Struct.*, 2021, **28**, 100188.
13 A. Lamy-Mendes, A. Dora, R. Pontinha, P. Alves, P. Santos and L. Durães, *Constr. Build. Mater.*, 2021, **286**, 122815.
14 A. Greszta, S. Krzemińska, G. Bartkowiak and A. Dąbrowska, *Int. J. Mater. Res.*, 2021, **112**, 164–172.
15 Y. Du and H. E. Kim, *Fash. Text.*, 2022, **9**, 23.
16 S. Malakooti, M. I. Hatamleh, R. Zhang, T. Taghvaee, M. Miller III, Y. Ren, N. Xiang, D. Qian, C. Sotiriou-Leventis, N. Leventis and H. Lu, *Soft Matter*, 2021, **17**, 4496–4503.
17 S. Chandrasekaran, J. Feaster, J. Ynzunza, F. Li, X. Wang, A. J. Nelson and M. A. Worsley, *ACS Mater. Au*, 2022, **2**, 596–601.
18 L. Peles-Strahl, Y. Persky and L. Elbaz, *SusMat*, 2023, **3**, 44–57.
19 X. Tan, J. Qin, Y. Li, Y. Zeng, G. Zheng, F. Feng and H. Li, *J. Hazard. Mater.*, 2020, **397**, 122786.
20 M. Tabata, I. Adachi, Y. Ishii, H. Kawai, T. Sumiyoshi and H. Yokogawa, *Nucl. Instrum. Methods Phys. Res., Sect. A*, 2010, **623**, 339–341.
21 H. W. Jones, *4th Int. Conf. Environ. Syst.*, 2018, 1–10.
22 P. Tsou, *J. Non-Cryst. Solids*, 1995, **186**, 415–427.
23 D. Brownlee, *Annu. Rev. Earth Planet. Sci.*, 2014, **42**, 179–205.
24 D. E. Brownlee, P. Tsou, D. Burnett, B. Clark, M. Hanner, F. Horz, J. Kissel, J. McDonnell, R. Newburn and S. Sandford, *Meteorit. Planet. Sci.*, 1997, **32**, A22.
25 J. P. Randall, M. A. B. Meador and S. C. Jana, *ACS Appl. Mater. Interfaces*, 2011, **3**, 613–626.
26 M. A. B. Meador, S. Wright, A. Sandberg, B. N. Nguyen, F. W. Van Keuls, C. H. Mueller, R. Rodríguez-Solís and F. A. Miranda, *ACS Appl. Mater. Interfaces*, 2012, **4**, 6346–6353.
27 S. M. Jones, *J. Sol-Gel Sci. Technol.*, 2006, **40**, 351–357.
28 N. Leventis, A. Palczer, L. McCorkle, G. Zhang and C. Sotiriou-Leventis, *J. Sol-Gel Sci. Technol.*, 2005, **35**, 99–105.
29 M.-A. Einarsrud and S. Haereid, *J. Sol-Gel Sci. Technol.*, 1994, **2**, 903–906.

30 S. S. Prakash, C. J. Brinker and A. J. Hurd, *J. Non-Cryst. Solids*, 1995, **190**, 264–275.
31 Y.-G. Kwon, S.-Y. Choi, E.-S. Kang and S.-S. Baek, *J. Mater. Sci.*, 2000, **35**, 6075–6079.
32 A. Venkateswara Rao, E. Nilsen and M.-A. Einarsrud, *J. Non-Cryst. Solids*, 2001, **296**, 165–171.
33 T. C. Almeida da Silva, L. Marchiori, B. Oliveira Mattos, S. Ullah, H. da S. Barud, R. Romano Domeneguetti, H. D. Rojas-Mantilla, M. V. Boldrin Zanoni, U. P. Rodrigues-Filho, E. P. Ferreira-Neto and S. J. L. Ribeiro, *ACS Appl. Mater. Interfaces*, 2023, **15**, 23146–23159.
34 Y. Wu, X. Wang and J. Shen, *J. Sol-Gel Sci. Technol.*, 2023, **106**, 360–380.
35 R. C. Walker, K. E. Penzer, J. L. Stokes, F. I. Hurwitz, H. Guo and J. K. Ferri, *Microporous Mesoporous Mater.*, 2023, **356**, 112552.
36 R. C. Walker, A. E. Potochniak, A. P. Hyer and J. K. Ferri, *Adv. Colloid Interface Sci.*, 2021, **295**, 102464.
37 G. Nassar, E. Daou, R. Najjar, M. Bassil and R. Habchi, *Carbon Trends*, 2021, **4**, 100065.
38 Y. Ge, T. Zhang, B. Zhou, H. Wang, Z. Zhang, J. Shen and A. Du, *J. Mater. Res.*, 2018, **33**, 2052–2061.
39 T. S. Tran, N. K. Dutta and N. R. Choudhury, *ACS Appl. Nano Mater.*, 2020, **3**, 11608–11619.
40 C. Zhu, T. Liu, F. Qian, T. Y. J. Han, E. B. Duoss, J. D. Kuntz, C. M. Spadaccini, M. A. Worsley and Y. Li, *Nano Lett.*, 2016, **16**, 3448–3456.
41 J. Yang, H. Wang, B. Zhou, J. Shen, Z. Zhang and A. Du, *Langmuir*, 2021, **37**, 2129–2139.
42 S. Bag, I. U. Arachchige and M. G. Kanatzidis, *J. Mater. Chem.*, 2008, **18**, 3628–3632.
43 B. J. Riley, J. Chun, J. V. V. Ryan, J. Matyáš, X. S. Li, D. W. Matson, S. K. Sundaram, D. M. Strachan and J. D. Vienna, *RSC Adv.*, 2011, **1**, 1704–1715.
44 J. L. Mohanan, I. U. Arachchige and S. L. Brock, *Science*, 2005, **307**, 397–400.
45 K. S. Subrahmanyam, D. Sarma, C. D. Malliakas, K. Polychronopoulou, B. J. Riley, D. A. Pierce, J. Chun and M. G. Kanatzidis, *Chem. Mater.*, 2015, **27**, 2619–2626.
46 Y. Guo, S. Qin, X. Yao, S. Liu, Z. Ji, Z. Ma and X. Wang, *J. Appl. Polym. Sci.*, 2022, **139**, e52891.
47 S. L. Vivod, M. Ann, B. Meador, C. Pugh, M. Wilkosz, K. Calomino and L. McCorkle, *ACS Appl. Mater. Interfaces*, 2020, **12**, 8622–8633.
48 A. Shinko, PhD Thesis, The University of Akron, 2015.
49 J. L. Cashman, B. N. Nguyen, B. Dosa and M. A. B. Meador, *ACS Appl. Polym. Mater.*, 2020, **2**, 2179–2189.
50 M. A. B. Meador, C. R. Alemán, K. Hanson, N. Ramirez, S. L. Vivod, N. Wilmoth and L. McCorkle, *ACS Appl. Mater. Interfaces*, 2015, **7**, 1240–1249.
51 S. L. Brock, in *Nanoscale Materials in Chemistry*, K. J. Klabunde and R. M. Richards, John Wiley & Sons, 2nd edn, 2009, pp. 209–241.
52 L. E. Nita, A. Ghilan, A. G. Rusu, I. Neamtu and A. P. Chiriac, *Pharmaceutics*, 2020, **12**, 449.
53 A. Iglesias-Mejuto and C. A. García-González, *Polymers*, 2022, **14**, 1211.
54 H. Cui, N. Wu, X. Ma and F. Niu, *Polym. Degrad. Stab.*, 2023, **207**, 110213.
55 Durable Polyimide Aerogels, **https://technology.nasa.gov/patent/LEW-TOPS-133**, 2021 (accessed 16 June 2023).
56 Z. Zhu, H. Yao, F. Wang, J. Dong, K. Wu, J. Cao and D. Long, *Macromol. Mater. Eng.*, 2019, **304**, 1800676.
57 D. A. Dornbusch, R. P. Viggiano, J. W. Connell, Y. Lin and V. F. Lvovich, *Electrochim. Acta*, 2022, **403**, 139406.
58 Q. Zhao, S. Stalin, C.-Z. Zhao and L. A. Archer, *Nat. Rev. Mater.*, 2020, **5**, 229–252.
59 R. M. Hensleigh, H. Cui, J. S. Oakdale, J. C. Ye, P. G. Campbell, E. B. Duoss, C. M. Spadaccini, X. Zheng and M. A. Worsley, *Mater. Horiz.*, 2018, **5**, 1035–1041.
60 A. Tang, J. Li, J. Li, S. Zhao, W. Liu, T. Liu, J. Wang and Y. Liu, *J. Biomater. Sci., Polym. Ed.*, 2019, **30**, 797–814.
61 V. B. Morris, S. Nimbalkar, M. Younesi, P. McClellan and O. Akkus, *Ann. Biomed. Eng.*, 2017, **45**, 286–296.
62 J. Feng, B. L. Su, H. Xia, S. Zhao, C. Gao, L. Wang, O. Ogbeide, J. Feng and T. Hasan, *Chem. Soc. Rev.*, 2021, **50**, 3842–3888.
63 P. Yan, E. Brown, Q. Su, J. Li, J. Wang, C. Xu, C. Zhou and D. Lin, *Small*, 2017, **13**, 1701756.
64 Q. Zhang, F. Zhang, S. P. Medarametla, H. Li, C. Zhou and D. Lin, *Small*, 2016, **12**, 1702–1708.
65 H. Tetik, Y. Wang, X. Sun, D. Cao, N. Shah, H. Zhu, F. Qian and D. Lin, *Adv. Funct. Mater.*, 2021, **31**, 2103410.
66 Y. Lin, F. Liu, G. Casano, R. Bhavsar, I. A. Kinloch and B. Derby, *Adv. Mater.*, 2016, **28**, 7993–8000.
67 S. Zhao, G. Siqueira, S. Drdova, D. Norris, C. Ubert, A. Bonnin, S. Galmarini, M. Ganobjak, Z. Pan and S. Brunner, *Nature*, 2020, **584**, 387–392.
68 Y. Lin, R. Yang and X. Wu, *RSC Appl. Polym.*, 2023, **1**, 132–157.
69 I. D. Robertson, M. Yourdkhani, P. J. Centellas, J. E. Aw, D. G. Ivanoff, E. Goli, E. M. Lloyd, L. M. Dean, N. R. Sottos and P. H. Geubelle, *Nature*, 2018, **557**, 223–227.
70 C. Zhang, J. Hao, W. Shi, Y. Su, K. Mitchell, W. Hua, W. Jin, S. Lee, L. Wen and Y. Jin, *Biofabrication*, 2023, **15**, 045015.
71 A. Aguzin, A. Dominguez-Alfaro, M. Criado-Gonzalez, S. Velasco-Bosom, M. L. Picchio, N. Casado, E. Mitoudi-Vagourdi, R. J. Minari, G. G. Malliaras and D. Mecerreyes, *Mater. Horiz.*, 2023, **10**, 2516–2524.
72 J. E. Aw, X. Zhang, A. Z. Nelson, L. M. Dean, M. Yourdkhani, R. H. Ewoldt, P. H. Geubelle and N. R. Sottos, *Adv. Mater. Technol.*, 2022, **7**, 2200230.
73 J. A. Lewis, *Adv. Funct. Mater.*, 2006, **16**, 2193–2204.
74 M. A. S. R. Saadi, A. Maguire, N. T. Pottackal, M. S. H. Thakur, M. Md. Ikram, A. J. Hart, P. M. Ajayan and M. M. Rahman, *Adv. Mater.*, 2022, **34**, 2108855.
75 S. Tagliaferri, A. Panagiotopoulos and C. Mattevi, *Mater. Adv.*, 2021, **2**, 540–563.
76 A. M'Barki, L. Bocquet and A. Stevenson, *Sci. Rep.*, 2017, **7**, 6017.

77 J. C. Conrad, S. R. Ferreira, J. Yoshikawa, R. F. Shepherd, B. Y. Ahn and J. A. Lewis, *Curr. Opin. Colloid Interface Sci.*, 2011, **16**, 71–79.
78 P. Wei, C. Cipriani, C.-M. Hsieh, K. Kamani, S. Rogers and E. Pentzer, *J. Appl. Phys.*, 2023, **134**, 100701.
79 A. Maguire, N. Pottackal, M. A. S. R. Saadi, M. M. Rahman and P. M. Ajayan, *Oxford Open Mater. Sci.*, 2017, **1**, itaa004.
80 R. G. Larson and Y. Wei, *J. Rheol.*, 2019, **63**, 477–501.
81 H. A. Barnes, *J. Non-Newtonian Fluid Mech.*, 1997, **70**, 1–33.
82 A. Katti, N. Shimpi, S. Roy, H. Lu, E. F. Fabrizio, A. Dass, L. A. Capadona and N. Leventis, *Chem. Mater.*, 2006, **18**, 285–296.
83 C. Feng and S.-S. Yu, *Polymers*, 2021, **13**, 3614.
84 C. Wang, S. Ma, D. Li, J. Zhao, H. Zhou, D. Wang, C. Liu, S. Wang and C. Chen, *Addit. Manuf.*, 2023, **70**, 103554.
85 Z. Ma, T. Xue, Q. Wali, Y. E. Miao, W. Fan and T. Liu, *Compos. Commun.*, 2023, **39**, 101528.
86 S. Chandrasekaran, B. Yao, T. Liu, W. Xiao, Y. Song, F. Qian, C. Zhu, E. B. Duoss, C. M. Spadaccini, Y. Li and M. A. Worsley, *Mater. Horiz.*, 2018, **5**, 1166–1175.
87 T. Wu, M. Ganobjak, G. Siqueira, Z. Zeng, M. Li, E. Filimonova, S. Saghamanesh, A. Bonnin, D. Sivaraman, J. Yip, L. Li, H. Wu, G. Nyström, W. J. Malfait and S. Zhao, *Adv. Mater. Technol.*, 2023, **8**, 2202155.
88 S. Qin, Y. Jiang, Z. Ji, C. Yang, Y. Guo, X. Zhang, H. Qin, X. Jia and X. Wang, *J. Appl. Polym. Sci.*, 2021, **138**, 50636.
89 D. A. Rau, J. Herzberger, T. E. Long and C. B. Williams, *ACS Appl. Mater. Interfaces*, 2018, **10**, 34828–34833.
90 ASTM D695-10, *Standard test method for compressive properties of rigid plastics, in Annual Book of ASTM Standards*, ASTM International, West Conshohocken, PA, 2010.
91 S. L. Vivod, M. A. B. Meador, A. Shinko, S. C. Jana and C. Pugh, *US Pat*, **10800883**, 2020.
92 Autodesk Inc., Tinkercad, tinkercad.com, (accessed 14 June 2023).
93 ASTM D7984-21, Standard test method for measurement of thermal effusivity of fabrics using a modified transient plane source (MTPS) instrument, in Annual Book of ASTM Standards, ASTM International, West Conshohocken, PA, 2021.
94 S. D. Kim, T. Byun, J. Kim, I. S. Chung and S. Kim, in *Polyimide for Electronic and Electrical Engineering Applications*, ed. S. Diaham, IntechOpen, 2021.
95 A. D. Adamczak, A. A. Spriggs, D. M. Fitch, W. Awad, C. A. Wilkie and J. C. Grunlan, *J. Appl. Polym. Sci.*, 2010, **115**, 2254–2261.
96 S. Malakooti, S. L. Vivod, M. Pereira, C. R. Ruggeri, D. M. Revilock, D. A. Scheiman, H. Guo, J. A. Salem, O. Benafan and J. C. Johnston, *Composites, Part B*, 2023, **260**, 110751.